



Oxidation Resistance of Ti-Al-Cr-Nb-Based High-Entropy Alloys in Air at 1073 K

Richard Gawel, Łukasz Rogal, and Kazimierz Przybylski

(Submitted July 29, 2018; in revised form May 14, 2019; published online June 27, 2019)

The effects of prolonged exposure to air at 1073 K on Al₂₀Cr₂₅Nb₂₀Ti₂₀Zr₁₅ and Al₂₀Cr₂₅Nb₁₉-Ti₂₀Zr₁₅Y₁ (at.%) high-entropy alloys (HEAs) were investigated in this work. Combined scanning electron microscopy and energy-dispersive x-ray spectroscopy (SEM–EDS) analysis revealed that scales containing all major elements in the systems are formed during the oxidation process. Thermogravimetric analysis carried out under the above-mentioned corrosive conditions indicates an initial parabolic kinetics course in the case of the sample with 1 at.% Y addition. However, after a certain period of time, the correlation between mass gain per unit surface area and time becomes linear. In the other case, oxidation proceeds according to the parabolic rate law for the entire process duration. The addition of 1 at.% Y decreases the parabolic rate constants by 1 order of magnitude, thereby improving the chemical stability of the studied Al-Cr-Nb-Ti-Zr system. This is confirmed by visual evaluation, as well as SEM–EDS cross-sectional analysis. Additionally, x-ray diffraction studies indicate that a multiphase oxide scale is formed on the metallic core of both samples. This means that selective oxidation does not occur and all constituent elements took part in the reaction. Taking all of the above into account, it can be concluded that more research is required to fully understand and improve the corrosion resistance of Ti-Al-Cr-Nb-based HEAs.

Keywords chemical analysis, high-entropy alloys, oxidation, oxide scales

1. Introduction

High-entropy alloys (HEAs) were first officially introduced to the scientific world in 2004 by Yeh and his team (Ref 1-4). These new materials can be defined as alloys that exhibit high configurational entropy (ΔS_{conf}) and consist of five or more principle elements in amounts that range between 5 and 35 at.%. Configurational entropy constitutes a large part of the mixing entropy (ΔS_{mix}). If the mixing entropy is sufficiently large, then the free enthalpy of mixing (ΔG_{mix}) can be below 0. This, in turn, leads to spontaneous formation of a single-phase alloy. The mixing enthalpy (ΔH_{mix}) value also influences the phenomenon, according to the following thermodynamic correlation:

$$\Delta G_{\text{mix}} = \Delta H_{\text{mix}} - T \cdot \Delta S_{\text{mix}} \quad (\text{Eq 1})$$

where T is the temperature [K]. The previously mentioned single phase that constitutes a HEA is usually a face-centered cubic (FCC) or body-centered cubic (BCC) crystalline structure. Configurational entropy depends on the principle element concentrations in accordance with the following equation:

$$\Delta S_{\text{conf}} = -R \sum X_i \ln X_i \quad (\text{Eq 2})$$

Richard Gawel and **Kazimierz Przybylski**, Faculty of Materials Science and Ceramics, AGH University of Science and Technology, Krakow, Poland; and **Łukasz Rogal**, Polish Academy of Sciences, Institute of Metallurgy and Materials, Krakow, Poland. Contact e-mail: ragaw@agh.edu.pl.

where R is the universal gas constant and X_i —atom fraction of principle element i . This approximation for liquid and solid alloys near the melting temperature suggests that maximum ΔS_{conf} can be obtained by mixing the elements together in equimolar ratios. However, non-equimolar compositions can also be classified as HEAs provided they meet the following criteria: $\Delta S_{\text{conf}} \geq 1.5R$ (Ref 5).

It has been determined that single-phase HEAs exhibit relatively high strength and ductility compared to traditional commercial alloys (Ref 3). Since then, HEAs have been seen as promising potential structural materials. They have also been considered for high-temperature applications due to their supposed sluggish diffusion kinetics and softening resistance at elevated temperatures (Ref 6, 7). This has led to high-temperature oxidation studies of several HEA systems, such as CoCrFeMnNi, AlCoCrFeNi and AlCoCrCuFeNi (Ref 8-14). These investigations have also been carried out on high-entropy materials consisting of elements that constitute refractory alloys, e.g., Ti, Ta, Mo, Nb, Hf, Cr and Zr (Ref 15-17). Aluminum has also often been added to refractory HEA systems in order to ensure better protection against high-temperature oxidizing conditions (Ref 18-20). This addition, however, still does not guarantee sufficient oxidation resistance against oxidizing atmospheres in the above-mentioned temperature range. For example, an equimolar NbMoCrTiAl HEA has exhibited oxidation that proceeds according to the linear rate law at 1173 and 1273 K (Ref 19). Other similar refractory HEAs demonstrated linear kinetics at 1573 K (Ref 20).

This work is an attempt at improving the oxidation resistance of refractory HEAs at temperatures below 1273 K. The effects of minor Si addition on the oxidation behavior of refractory HEAs have already been tested (Ref 19, 20). However, there are still not much data pertaining to active element dopant (e.g., Y, La) influence on the physicochemical properties of these alloys. Thus, the goal of this work is to investigate the chemical stability of an Al-Cr-Ti-Zr-Nb HEA in

air atmosphere at 1073 K and determine the effects of an active element dopant (1 at.% Y) on its high-temperature oxidation resistance.

2. Experimental Materials and Methods

HEAs, the designations and average chemical compositions of which are provided in Table 1, were prepared from elements of 99.99 wt.% purity in an arc melting furnace with a water-cooled copper plate under protective argon atmosphere. Details of the procedure can be found in Ref 21. After grinding, polishing and ultrasonic cleaning in acetone, the obtained HEA samples were inserted into the thermogravimetric apparatus schematically presented in (Ref 22). This setup enabled measurements of mass change as a function of time using a CI Precision Mk2 microbalance with 0.1 μg sensitivity and 1 μg accuracy. The materials were then exposed to air at 1073 K. Thermogravimetric analysis of the Al₂₀Cr₂₅Nb₂₀Ti₂₀Zr₁₅ alloy was carried out for 24 h, whereas the Al₂₀Cr₂₅Nb₂₀Ti₂₀Zr₁₅Y₁ HEA was subjected to both 24- and 48-h oxidation. The second material was also oxidized at 1023 and 1123 K in order to analyze the influence of temperature on growth kinetics. Information on the morphology and chemical composition of the samples after the above-mentioned procedures was then obtained using scanning electron microscopy (SEM; FEI SEM XL30 scanning electron microscope) combined with energy-dispersive x-ray spectroscopy (EDS; EDAX GEMINI 4000 spectrometer) using a Si(Li) detector with SUTW window. Additionally, x-ray diffraction (XRD) analysis was performed using a Philips PW 1410 diffractometer with CoK α filtered radiation. Scans were performed on polished cross-sectioned samples at 20° to 120°, with a step size of 0.02° and a dwell time of 5 s. Finally, a thin cross section of a selected sample was prepared using a focused ion beam (FIB; Hitachi FB-2000A FIB). The cross section was then observed by means of transmission electron microscopy (TEM; TOPCON EM-002B transmission electron microscope) at 400 kV accelerating voltage, and chemical composition point analysis was carried out using the EDS technique with a Si(Li) detector (Noran Instruments Energy Dispersive x-ray Spectrometer MODEL 623 M-3SPT).

3. Results and Discussion

Mass change per unit surface area as a function of oxidation time for both Al₂₀Cr₂₅Nb₂₀Ti₂₀Zr₁₅ and Al₂₀Cr₂₅Nb₁₉Ti₂₀Zr₁₅Y₁ HEAs is illustrated for both samples in Fig. 1. From this figure, it follows that, in the case of the first sample,

Table 1 Designation and average chemical composition of the studied high-entropy alloys

Designation	Element, at.%					
	Al	Cr	Nb	Ti	Zr	Y
Al ₂₀ Cr ₂₅ Nb ₂₀ Ti ₂₀ Zr ₁₅	20	25	20	20	15	...
Al ₂₀ Cr ₂₅ Nb ₁₉ Ti ₂₀ Zr ₁₅ Y ₁	20	25	19	20	15	1

mass change as a function of reaction time initially follows the parabolic rate law, and then, the correlation becomes linear after a certain period of time. On the other hand, the mass increase in the yttrium-containing sample remains parabolic throughout the entire oxidation process. This is confirmed from the linear regression performed on the curves representing the square of mass change per unit surface area as a function of time illustrated in Fig. 2. This suggests that the scale grown on Al₂₀Cr₂₅Nb₁₉Ti₂₀Zr₁₅Y₁ alloy exhibits better protective properties than that formed on Al₂₀Cr₂₅Nb₂₀Ti₂₀Zr₁₅. In both cases, the values of the rate constants, provided in Table 2, change after certain durations. It can be speculated that this is due to the changes in the rate-limiting reaction during the oxidation procedure after certain periods of time. However, further studies are necessary to determine this with certainty. From the determined rate constants, it follows that the addition of 1 at.% yttrium into the sample improves the oxidation

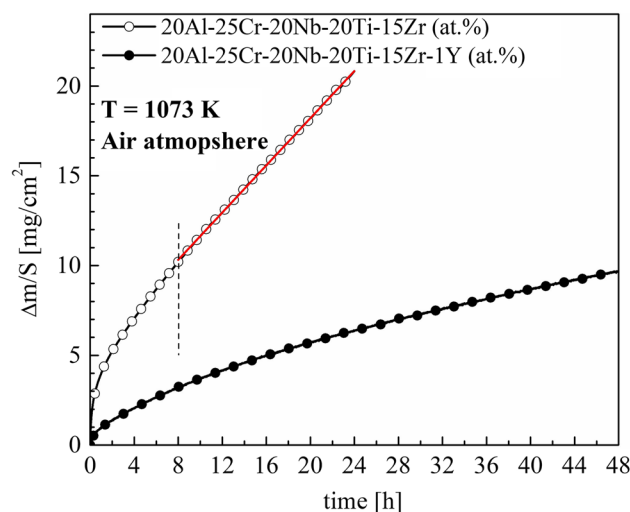


Fig. 1 Comparison of the oxidation kinetics curves obtained for Al₂₀Cr₂₅Nb₂₀Ti₂₀Zr₁₅ and Al₂₀Cr₂₅Nb₁₉Ti₂₀Zr₁₅Y₁ alloy after 24- and 48-h oxidation at 1073 K in air, respectively

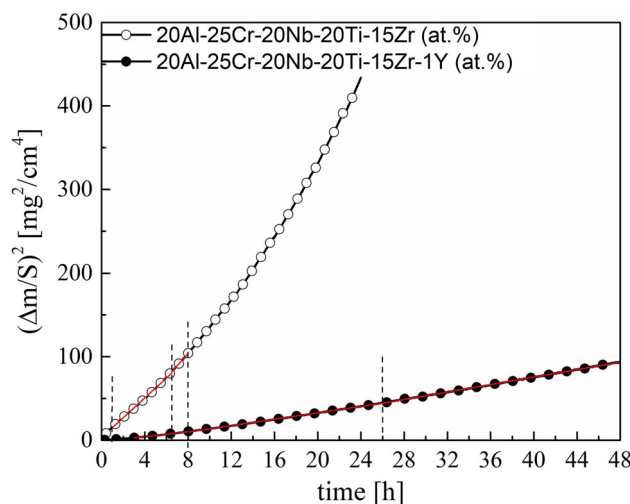


Fig. 2 Square of weight gain per unit surface area vs. oxidation time of Al₂₀Cr₂₅Nb₂₀Ti₂₀Zr₁₅ and Al₂₀Cr₂₅Nb₁₉Ti₂₀Zr₁₅Y₁ alloy

Table 2 Rate constant values obtained from oxidation kinetics analysis performed on Al₂₀Cr₂₅Nb₂₀Ti₂₀Zr₁₅ for 24 h and Al₂₀Cr₂₅Nb₁₉Ti₂₀Zr₁₅Y₁ for 48 h in air at 1073 K

Designation	Period of time	Rate law	Rate constant
Al ₂₀ Cr ₂₅ Nb ₂₀ Ti ₂₀ Zr ₁₅	1-6.5 h	Parabolic	$3.30 \cdot 10^{-9} \pm 4.95 \cdot 10^{-12}, \text{g}^2 \text{cm}^{-4} \text{s}^{-1}$
	6.5-8 h	Parabolic	$4.03 \cdot 10^{-9} \pm 4.42 \cdot 10^{-12}, \text{g}^2 \text{cm}^{-4} \text{s}^{-1}$
	8-24 h	Linear	$1.82 \cdot 10^{-7} \pm 5.17 \cdot 10^{-11}, \text{g} \text{cm}^{-2} \text{s}^{-1}$
Al ₂₀ Cr ₂₅ Nb ₁₉ Ti ₂₀ Zr ₁₅ Y ₁	3-8 h	Parabolic	$4.07 \cdot 10^{-10} \pm 1.35 \cdot 10^{-12}, \text{g}^2 \text{cm}^{-4} \text{s}^{-1}$
	8-25 h	Parabolic	$5.34 \cdot 10^{-10} \pm 4.36 \cdot 10^{-13}, \text{g}^2 \text{cm}^{-4} \text{s}^{-1}$
	25-48 h	Parabolic	$6.22 \cdot 10^{-10} \pm 4.27 \cdot 10^{-13}, \text{g}^2 \text{cm}^{-4} \text{s}^{-1}$

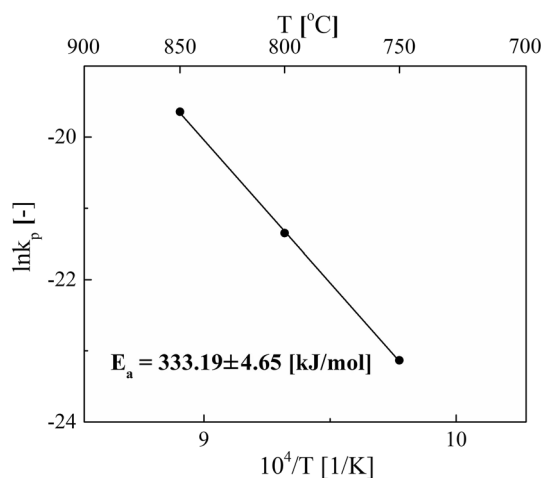


Fig. 3 Temperature dependence of parabolic rate constants obtained for Al₂₀Cr₂₅Nb₁₉Ti₂₀Zr₁₅Y₁ alloy after 48-h oxidation at 1023, 1073 and 1123 K in air

kinetics by 1 order of magnitude. This indicates a very positive effect of the dopant on the oxidation kinetics of the studied HEA system at 1073 K. Still, oxidation mechanism investigations are required to give a detailed explanation for this beneficial influence.

Information on temperature dependence of the parabolic rate constants determined at 1023, 1073 and 1123 K after a certain initial period up to ~ 24 h is provided for the yttrium-doped sample in Fig. 3. Linear regression of the obtained data reveals that the activation energy of the process during the aforementioned period of oxidation is 333.19 ± 4.65 [kJ/mol]. Similar values can be determined from the same analysis of other time periods of the high-temperature oxidation process, i.e., 331.94 ± 8.63 [kJ/mol] up to ~ 35 h and 327.85 ± 28.41 [kJ/mol] for the remaining duration. These values are slightly higher than those determined for a non-high-entropy TiAlNb-based alloy in the temperature range of 1148-1248 K (304 [kJ/mol]) (Ref 23) and an Al_{0.1}CoCrFeNi HEA in the temperature range of 973-1173 K (280.68 kJ/mol) (Ref 24). The relatively high activation energy values can probably be attributed to the sluggish diffusion effect in HEAs mentioned in the Introduction section of this work. However, further studies are necessary to state this with absolute certainty.

Surface morphologies of the Al₂₀Cr₂₅Nb₂₀Ti₂₀Zr₁₅ and Al₂₀Cr₂₅Nb₁₉Ti₂₀Zr₁₅Y₁ samples after 24-h oxidation at 1073 K in air are shown in Fig. 4(a) and (b), respectively. From these SEM observations, it follows that a non-continuous outer layer built of small grains was formed on the surface of each sample during the oxidation process. The microstructure of the

outer layer illustrated in Fig. 4(a) consists of small grains, which form larger aggregates in some areas. On the other hand, the grains in Fig. 4(b) are somewhat larger and far less aggregation is visible. The reason for this is unknown and requires further studies.

In order to determine the differences in chemical composition between the outer non-continuous layer and the remaining visible surface, EDS point analysis was carried out on the oxidized Al₂₀Cr₂₅Nb₂₀Ti₂₀Zr₁₅ alloy. The points selected for chemical composition studies are shown in the microphotograph illustrated in Fig. 5(a). The respective EDS spectra obtained at these points are shown in Fig. 5(b), (c) and (d). All the constituent elements were detected in each case (Fig. 5(b) (c) and (d). However, the presence of oxygen below the non-continuous layer on the surface (Fig. 5d) suggests that the oxide scale grown on the metallic substrate during the oxidation process not only consists of the non-continuous outer layer, but of an additional inner layer as well. The same conclusion can be obtained from EDS point analysis performed on the Al₂₀Cr₂₅Nb₁₉Ti₂₀Zr₁₅Y₁ alloy after 24-h oxidation shown in Fig. 6(a). The obtained results are qualitatively illustrated by the EDS spectra in Fig. 6(b), (c) and (d) for points 1, 2 and 3, respectively. The chemical compositions determined by the EDS point analysis performed on both samples after oxidation are listed in Table 3. From this table, it follows that all the constituent elements were detected in both scale layers on each sample. However, greater chromium content and lower amounts of titanium were determined in the inner layer compared to the outer scale layer. This suggests the formation of more significant amounts of Cr-containing compounds and less compounds with Ti in the inner layer of the scale.

Cross-sectional SEM analysis of the Al₂₀Cr₂₅Nb₂₀-Ti₂₀Zr₁₅ material combined with EDS line scan studies is presented in Fig. 7(a) and (b), respectively. From the obtained SEM microphotograph, it follows that a ~ 38 - μm -thick oxide scale was grown during oxidation at 1073 K. The image also indicates a significant formation of oxides inside the metallic substrate, which makes it difficult to precisely determine the scale/substrate interface. EDS analysis provided in Fig. 7(b) indicates predominant amounts of Cr and Ti at the gas/scale interface that rapidly decrease ~ 10 μm along with distance from the surface. On the other hand, there is lower Nb and Zr content at the surface and Al at the interface is practically not observed. These elements increase along with depth for the initial ~ 10 μm . The EDS results are difficult to interpret as there are several maxima pertaining to individual elements inside the oxide scale. First, maxima pertaining to Cr and Zr are observed at the same depth. Then, at a slightly deeper position inside the scale, maxima of Nb and Ti are determined. It is interesting to notice that below ~ 15 μm the courses of Cr and Zr distribution are similar, yet the detected Zr concentration is

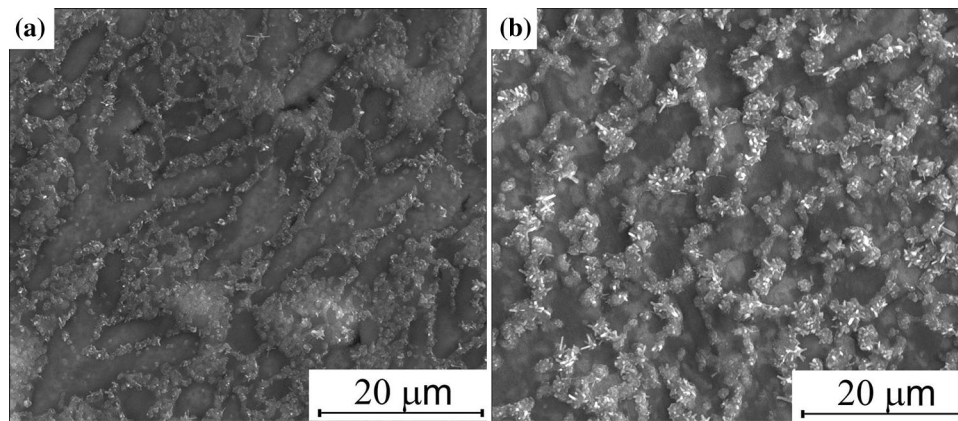


Fig. 4 SEM analysis performed on the (a) Al₂₀Cr₂₅Nb₂₀Ti₂₀Zr₁₅ and (b) Al₂₀Cr₂₅Nb₁₉Ti₂₀Zr₁₅Y₁ alloy after 24-h oxidation at 1073 K in air

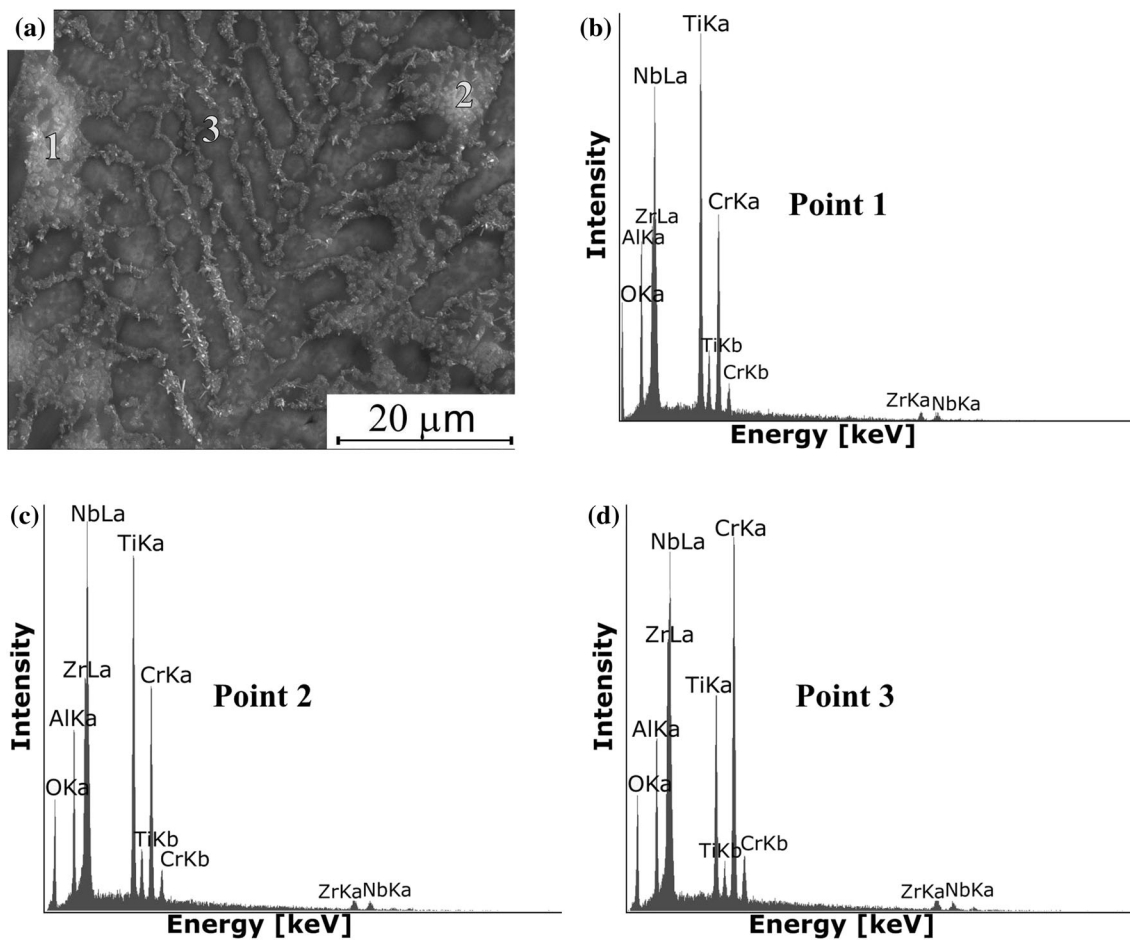


Fig. 5 EDS point analysis of the oxidized Al₂₀Cr₂₅Nb₂₀Ti₂₀Zr₁₅ sample: (a) SEM image illustrating locations of EDS point analysis, (b) EDS analysis of point 1, (c) EDS analysis of point 2 and (d) EDS analysis of point 3

higher than that of Cr. The same is true for Ti and Nb. As for Al, while some maxima are observed, the detected amounts of this element generally increase steadily as the analysis approaches the metallic core. Oxygen distribution results show that a rapid decrease in the element is observed between 30 and 38 μm , suggesting that below the latter depth the material becomes metallic. However, a significant oxygen concentration

was still determined in the EDS analysis. It can be speculated that this is the result of insufficient protection from the scale, as well as internal oxidation taking place during exposure to air atmosphere at 1073 K. Still, further studies are necessary to confirm this.

As for the Al₂₀Cr₂₅Nb₁₉Ti₂₀Zr₁₅Y₁ sample, cross-sectional SEM analysis is illustrated in Fig. 8(a), whereas EDS line

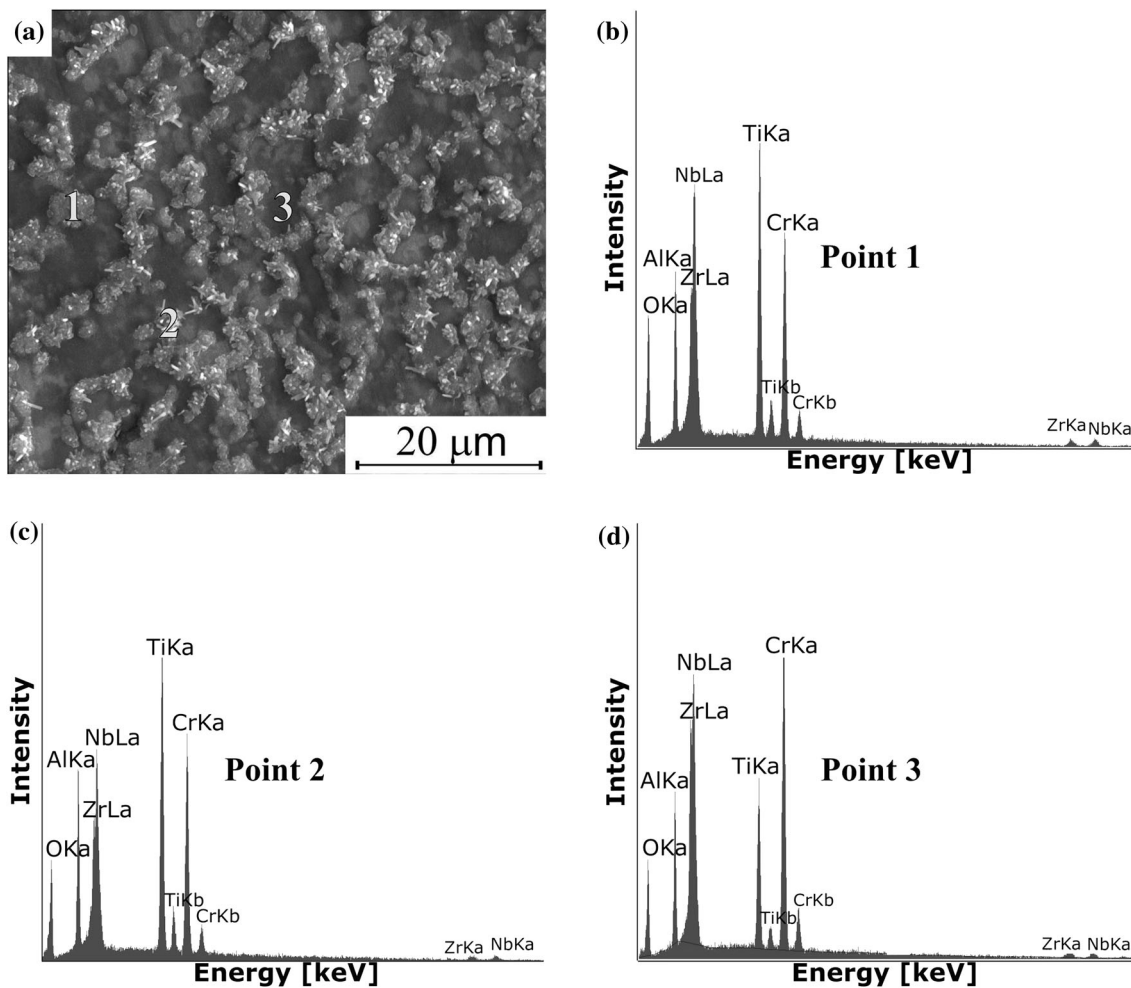


Fig. 6 EDS point analysis of the Al₂₀Cr₂₅Nb₁₉Ti₂₀Zr₁₅Y₁ sample after 24-h oxidation at 1073 K in air: (a) SEM image illustrating locations of EDS point analysis, (b) EDS analysis of point 1, (c) EDS analysis of point 2 and (d) EDS analysis of point 3

Table 3 Chemical compositions determined by EDS point analysis performed on the surface of the Al₂₀Cr₂₅Nb₂₀Ti₂₀Zr₁₅ and Al₂₀Cr₂₅Nb₁₉Ti₂₀Zr₁₅Y₁ high-entropy alloys after 24-h oxidation at 1073 K in air

Analyzed SEM image	Point selected for EDS analysis	Element, at.%					
		O	Al	Cr	Nb	Ti	Zr
Figure 5(a)	1	51.9 ± 1.9	11.0 ± 1.5	9.3 ± 1.1	7.7 ± 4.7	14.4 ± 0.8	5.3 ± 4.9
	2	51.2 ± 1.9	10.7 ± 1.5	9.5 ± 1.1	8.3 ± 4.6	13.4 ± 0.9	6.4 ± 4.4
	3	49.2 ± 1.8	10.7 ± 1.5	16.0 ± 0.8	7.3 ± 4.9	7.5 ± 1.2	9.1 ± 3.6
Figure 6(a)	1	58.0 ± 1.6	10.4 ± 1.4	9.2 ± 1.0	6.6 ± 4.8	11.0 ± 0.8	4.7 ± 3.4
	2	51.4 ± 1.7	14.8 ± 1.2	11.5 ± 0.9	4.7 ± 3.4	13.3 ± 0.8	4.1 ± 2.7
	3	47.5 ± 1.9	11.7 ± 1.5	16.9 ± 0.8	7.7 ± 5.3	7.5 ± 1.2	8.7 ± 4.1

scan studies are presented in Fig. 8(b). From this microphotograph, it follows that an oxide scale of ~ 66 μm thickness was formed in this case. This larger thickness compared to the previous case could be the result of better scale/substrate adherence; however, this is only an assumption at this point of research. The element distribution inside the oxide scale is, once again, very complex and requires further studies. As in the previous case, greater Ti and Cr concentrations are observed at the scale/gas interface compared to the other elements

(Fig. 7b). The content of these elements initially decreases about 7 μm, whereas the concentrations of the remaining elements increase. Oxygen concentration around the previously mentioned depth achieves a maximum, after which the content of that element steadily decreases. At around 34 μm depth, maxima of Cr and Zr content along with minimal Ti concentration can be observed. Oxygen and niobium distribution curves also exhibit a minimum. The reason for this is unknown and requires further studies. The plots pertaining to

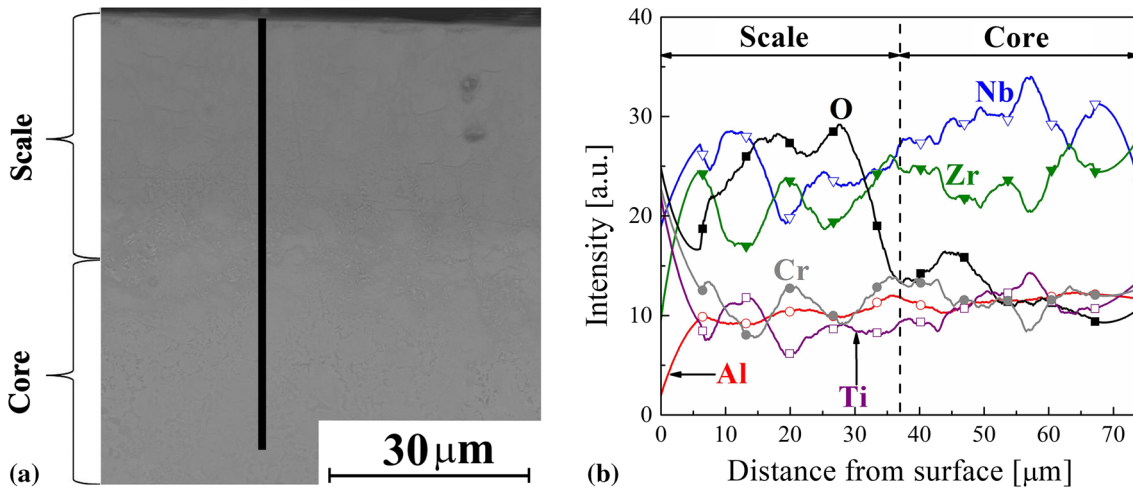


Fig. 7 (a) SEM cross-sectional microphotograph of the Al₂₀Cr₂₅Nb₂₀Ti₂₀Zr₁₅ sample after oxidation at 1073 K in air for 24 h and (b) EDS line scan results obtained from analysis of the cross section

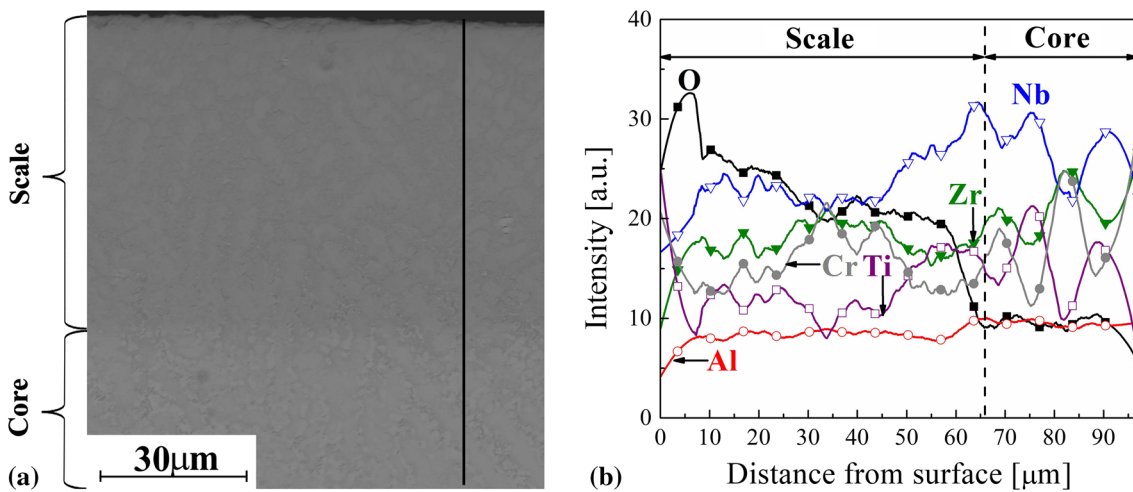


Fig. 8 (a) SEM cross-sectional microphotograph of the Al₂₀Cr₂₅Nb₁₉Ti₂₀Zr₁₅Y₁ sample after oxidation at 1073 K in air for 24 h and (b) EDS line scan results obtained from analysis of the cross section

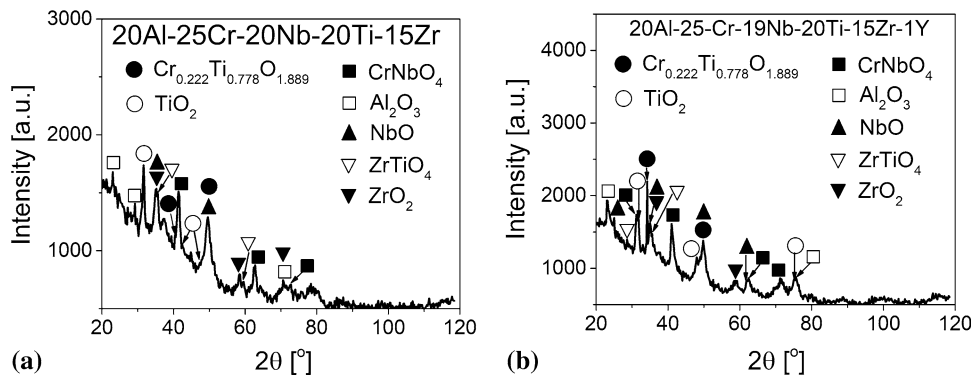


Fig. 9 XRD pattern of the (a) Al₂₀Cr₂₅Nb₂₀Ti₂₀Zr₁₅ and (b) Al₂₀Cr₂₅Nb₁₉Ti₂₀Zr₁₅Y₁ sample after oxidation at 1073 K in air for 24 h

Cr and Zr distribution are similar to those obtained for the previous sample; however, the concentrations of both elements in the scale are more comparable. The Ti and Nb distributions

are also similar; however, much higher Nb content was detected throughout the scale. As in the previous case, Al content steadily increases as the analysis approaches the core/scale

interface and is relatively low compared to the other elements. As for oxygen, while a rapid decrease is observed between 57 and 66 μm , some amounts of the element are still detected in the metallic core. This suggests that the protection against high-temperature corrosion in air provided by the scale was not entirely sufficient. However, the oxygen concentration appears to quickly diminish at depths below $\sim 90 \mu\text{m}$.

XRD analysis of the $\text{Al}_{20}\text{Cr}_{25}\text{Nb}_{20}\text{Ti}_{20}\text{Zr}_{15}$ and $\text{Al}_{20}\text{Cr}_{25}\text{Nb}_{19}\text{Ti}_{20}\text{Zr}_{15}\text{Y}_1$ samples after oxidation (Fig. 9a and b, respectively) reveals that the scales formed on the aforementioned alloys consist of several phases including Al_2O_3 and TiO_2 , as well as other oxides and spinels. This confirms that selective oxidation does not take place in either case and each major component in the HEAs takes part in the reaction with oxygen at 1073 K. From this, it can be concluded that high-temperature oxidation of the Al-Cr-Nb-Ti-Zr HEA system is a very complex process and requires further investigations. It can also be seen that the yttrium dopant does not seem to significantly influence the phase composition of the scale.

Further information on the $\text{Al}_{20}\text{Cr}_{25}\text{Nb}_{19}\text{Ti}_{20}\text{Zr}_{15}\text{Y}_1$ sample after 24-h oxidation at 1073 K was obtained from TEM-EDS analysis of a FIB-prepared cross section. The TEM image (Fig. 10) confirms that the sample is built of different phases. The EDS results (Table 4) also indicate that minor amounts of an yttrium oxide phase, undetected by XRD analysis, form at certain locations inside the oxidized material. The exact influence of this phenomenon on the diffusion of elements in the HEA during high-temperature oxidation has yet to be determined and requires further investigations. As for the

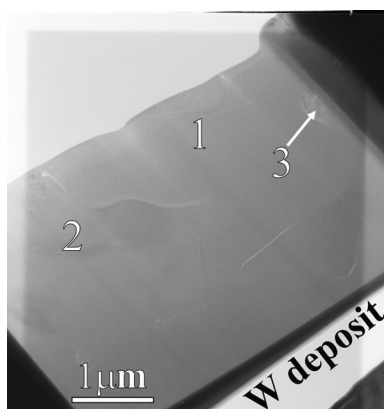


Fig. 10 TEM cross-sectional image of the $\text{Al}_{20}\text{Cr}_{25}\text{Nb}_{19}\text{Ti}_{20}\text{Zr}_{15}\text{Y}_1$ alloy after 24-h oxidation in air at 1073 K

other EDS results, at point 1 an oxide phase containing significant amounts of Cr and Zr was determined, whereas at point 2 mostly Nb, Ti and Al were detected along with oxygen.

The initial studies presented above indicate that the oxidation of Al-Cr-Nb-Ti-based HEAs is non-selective and all constituent elements contribute to scale formation. Similar phases are present in the mixed oxide scales determined after oxidation of other Al-Cr-Nb-Ti HEAs (Ref 19, 20). Those studies indicate that the layers grown on those materials provide insufficient protection against oxidizing atmospheres at elevated temperatures. Furthermore, internal precipitates can be formed during prolonged high-temperature oxidation (Ref 19). The oxygen distribution determined in this work suggests that the aforementioned internal corrosion took place during exposure of the investigated alloys to synthetic air at 1073 K.

The beneficial influence of Si addition has been attributed to the formation of a $(\text{Nb,Ti})_5\text{Si}_3$ phase (Ref 20), which has been known to act as an oxygen diffusion barrier in refractory metal solid solutions (Ref 25). Other studies suggest that the presence of Si in the refractory HEA system facilitates the formation of an aluminum-rich oxide scale (Ref 19). In the case of 1 at.% Y addition, however, a significant increase in Al inside the scale was not observed. Additional phases were also not detected by XRD analysis after oxidation. The beneficial effect of yttrium addition seems to be associated with ensuring growth of a thicker oxide scale that provides better protection against oxygen diffusion. Any further effects this element might have on high-temperature oxidation can only be speculated at this stage of research. Thus, determining the influence 1 at.% Y can have scale/substrate adherence and the oxidation mechanism of Ti-Al-Cr-Nb-based HEAs will be the subject of future studies. Furthermore, phase composition analysis will also be carried out on the initial Al-Cr-Nb-Ti-Zr HEAs before oxidation in order to determine whether the structures that constitute the material remain similar to those determined for other refractory HEAs containing Ti, Nb and Zr (Ref 26, 27).

4. Summary

From all the obtained initial results, it can be concluded that much work is still needed before the studied HEA materials capable of operating at high temperatures in corrosive atmospheres are fully understood or ready for practical use. The fact that all the constituent elements of the Ti-Al-Cr-Nb-based HEAs react with oxygen during oxidation at 1073 K indicates that the chemical stability of the samples at elevated temperatures requires improvement. Furthermore, the presence of all the elements is determined throughout the entire scale. This means that oxide mixtures can be found throughout the entire

Table 4 Chemical compositions determined by EDS point analysis performed on an FIB-prepared cross section of $\text{Al}_{20}\text{Cr}_{25}\text{Nb}_{19}\text{Ti}_{20}\text{Zr}_{15}\text{Y}_1$ high-entropy alloy after 24-h oxidation at 1073 K in air

Analyzed image	SEM	Point selected for EDS analysis	Element, at.%						
			O	Al	Cr	Nb	Ti	Zr	Y
Figure 10		1	48.5 ± 2.2	6.0 ± 1.1	14.0 ± 0.6	9.4 ± 0.8	5.5 ± 0.5	16.4 ± 1.4	0.2 ± 0.1
		2	37.5 ± 1.2	11.1 ± 0.6	6.0 ± 0.3	20.6 ± 0.7	19.1 ± 0.5	5.5 ± 0.6	0.2 ± 0.1
		3	44.4 ± 1.3	12.0 ± 0.8	0.7 ± 0.1	0.7 ± 0.1	0.6 ± 0.1	2.2 ± 0.4	39.5 ± 1.3

scale. Doping the materials with an active element seems to have a positive influence on the scale properties; however, more studies are necessary to fully comprehend the reason behind this. Methods for obtaining greater Al_2O_3 and Cr_2O_3 content in the scale and restricting the reactivity of the remaining HEA elements must be researched before these alloys can be used in high-temperature conditions. Methods of further improving the chemical stability properties of the materials while maintaining good material strength and plasticity will be the subject of future studies.

Acknowledgments

The research leading to these results received funding from Polish science financial resources and the National Science Centre, Poland, Project title: “Development of new HEAs with dominant content of hexagonal solid solutions,” Project no: UMO-2014/15/D/ST8/02638, and was also carried out as part of the statutory activities of the Department of Physical Chemistry and Modelling, Faculty of Materials Science and Ceramics, AGH University of Science and Technology (Contract No. 11.11.160.768).

Open Access

This article is distributed under the terms of the Creative Commons Attribution 4.0 International License (<http://creativecommons.org/licenses/by/4.0/>), which permits unrestricted use, distribution, and reproduction in any medium, provided you give appropriate credit to the original author(s) and the source, provide a link to the Creative Commons license, and indicate if changes were made.

References

1. T.K. Chen, T.-T. Shun, J.-W. Yeh, and M.S. Wong, Nanostructured Nitride Films of Multi-Element High-Entropy Alloys by Reactive DC Sputtering, *Surf. Coat. Technol.*, 2004, **188–189**, p 193–200
2. P.-K. Huang, J.-W. Yeh, T.-T. Shun, and S.-K. Chen, Multi-Principal-Element Alloys with Improved Oxidation and Wear Resistance for Thermal Spray Coating, *Adv. Eng. Mater.*, 2004, **6(1–2)**, p 74–78
3. J.-W. Yeh, S.-K. Chen, S.-J. Lin, J.-Y. Gan, T.-S. Chin, T.-T. Shun, C.-H. Tsau, and S.-Y. Chang, Nanostructured High-Entropy Alloys with Multiple Principal Elements: Novel Alloy Design Concepts and Outcomes *Adv. Eng. Mater.*, 2004, **6(5)**, p 299–303
4. C.-Y. Hsu, J.-W. Yeh, S.-K. Chen, and T.-T. Shun, Wear Resistance and High-Temperature Compression Strength of Fcc $\text{CuCoNiCrAl}_{0.5}\text{Fe}$ Alloy with Boron Addition, *Metall. Mater. Trans. A*, 2004, **35(5)**, p 1465–1469
5. D.B. Miracle, J.D. Miller, O.N. Senkov, C. Woodward, M.D. Uchic, and J. Tiley, Exploration and Development of High Entropy Alloys for Structural Applications, *Entropy*, 2014, **16(1)**, p 494–525
6. Z.P. Lu, H. Wang, M.W. Chen, I. Baker, J.W. Yeh, C.T. Liu, and T.G. Nieh, An Assessment on the Future Development of High-Entropy Alloys: Summary from a Recent Workshop, *Intermetallics*, 2015, **66**, p 67–76
7. K.Y. Tsai, M.H. Tsai, and J.W. Yeh, Sluggish Diffusion in Co-Cr-Fe-Mn-Ni high-entropy alloys, *Acta Mater.*, 2013, **61(13)**, p 4887–4897
8. W. Kai, C.C. Li, F.P. Cheng, K.P. Chu, R.T. Huang, L.W. Tsay, and J.J. Kai, The Oxidation Behavior of an Equimolar FeCoNiCrMn High-Entropy Alloy at 950 C in Various Oxygen-Containing Atmospheres, *Corros. Sci.*, 2016, **108**, p 209–214
9. G. Laplanche, U.F. Volkert, G. Eggeler, and E.P. George, Oxidation Behavior of the CrMnFeCoNi High-Entropy Alloy, *Oxid. Metals*, 2016, **85(5–6)**, p 629–645

10. T.M. Butler and M.L. Weaver, Oxidation Behavior of Arc Melted AlCoCrFeNi Multi-Component High-Entropy Alloys, *J. Alloy. Compd.*, 2016, **674**, p 229–244
11. T.M. Butler, J.P. Alfano, R.L. Martens, and M.L. Weaver, High-Temperature Oxidation Behavior of Al-Co-Cr-Ni-(Fe or Si) Multicomponent High-Entropy Alloys, *JOM*, 2015, **67(1)**, p 246–259
12. H.M. Daoud, A.M. Manzoni, R. Volkl, N. Wanderka, and U. Glatzel, Oxidation Behavior of $\text{Al}_8\text{Co}_{17}\text{Cr}_{17}\text{Cu}_8\text{Fe}_{17}\text{Ni}_{33}$, $\text{Al}_{23}\text{Co}_{15}\text{Cr}_{23}\text{Cu}_8\text{Fe}_{15}\text{Ni}_{15}$, and $\text{Al}_{17}\text{Co}_{17}\text{Cr}_{17}\text{Cu}_{17}\text{Fe}_{17}\text{Ni}_{17}$ Compositionally Complex Alloys (high-entropy alloys) at Elevated Temperatures in Air, *Adv. Eng. Mater.*, 2015, **17(8)**, p 1134–1141
13. L. Chen, Z. Zhou, Z. Tan, D. He, K. Bobzin, L. Zhao, M. Öte, and T. Königstein, High Temperature Oxidation Behavior of $\text{Al}_{0.6}\text{CrFeCoNi}$ and $\text{Al}_{0.6}\text{CrFeCoNiSi}_{0.3}$ High Entropy Alloys, *J. Alloy. Compd.*, 2018, **764**, p 845–852
14. J. Dąbrowa, G. Cieślak, M. Stygar, K. Mroczka, K. Berent, T. Kulik, and M. Danielewski, Influence of Cu Content on High Temperature Oxidation Behavior of $\text{AlCoCrCu}_x\text{FeNi}$ High Entropy Alloys ($x = 0; 0.5; 1$), *Intermetallics*, 2017, **84**, p 52–61
15. O.N. Senkov, S.V. Senkova, D.M. Dimiduk, C. Woodward, and D.B. Miracle, Oxidation Behavior of a Refractory NbCrMo $_{0.5}$ Ta $_{0.5}$ TiZr Alloy, *J. Mater. Sci.*, 2012, **47(18)**, p 6522–6534
16. B. Gorr, M. Azim, H.J. Christ, T. Mueller, D. Schliephake, and M. Heilmaier, Phase Equilibria, Microstructure, and High Temperature Oxidation Resistance of Novel Refractory High-Entropy Alloys, *J. Alloy. Compd.*, 2015, **624**, p 270–278
17. S. Sheikh, M.K. Bijaksana, A. Motallebzadeh, S. Shafeie, A. Lozinko, L. Gan, T.-K. Tsao, U. Klement, D. Canadinc, H. Murakami, and S. Guo, Accelerated Oxidation in Ductile Refractory High-Entropy Alloys, *Intermetallics*, 2018, **97**, p 58–66
18. S. Sheikh, L. Gan, T.-K. Tsao, H. Murakami, S. Shafeie, and S. Guo, Aluminumizing for Enhanced Oxidation Resistance of Ductile Refractory High-Entropy Alloys, *Intermetallics*, 2018, **103**, p 40–51
19. B. Gorr, F. Mueller, H.-J. Christ, T. Mueller, H. Chen, A. Kauffmann, and M. Heilmaier, High Temperature Oxidation Behavior of an Equimolar Refractory Metal-Based Alloy 20Nb-20Mo-20Cr-20Ti-20Al with and Without Si Addition, *J. Alloys Compd.*, 2016, **688(Part B)**, p 468–477
20. C.M. Liu, H.M. Wang, S.Q. Zhang, H.B. Tang, and A.L. Zhang, Microstructure and Oxidation Behavior of New Refractory High Entropy Alloys, *J. Alloys Compd.*, 2014, **583**, p 162–169
21. Ł. Rogal, J. Morgiel, Z. Swiatek, and F. Czerwinski, Microstructure and Mechanical Properties of the New Nb $_{25}$ Sc $_{25}$ Ti $_{25}$ Zr $_{25}$ Eutectic High Entropy Alloy, *Mater. Sci. Eng. A*, 2016, **651**, p 590–597
22. S. Mrowec and Z. Grzesik, Oxidation of Nickel and Transport Properties of Nickel Oxide, *J. Phys. Chem. Solids*, 2004, **65**, p 1651–1657
23. J. Małecka, Oxidation Activation Energy of Titanium Alloy Based on TiAl(γ) Intermetallic Phase, *Adv. Mater. Sci.*, 2018, **18**, p 5–14
24. H.S. Grewal, R.M. Sanjiv, H.S. Arora, R. Kumar, A. Ayyagari, S. Mukherjee, and H. Singh, Activation Energy and High Temperature Oxidation Behavior of Multi-Principal Element Alloy, *Adv. Eng. Mater.*, 2017, **19(1700182)**, p 1–5
25. B. Xiong, C. Cai, H. Wan, and Y. Zheng, Effects of Si, W and W-Mo on Isothermal Oxidation Behaviors of Nb/Nb $_{5}$ Si $_{3}$ In Situ Composites at High Temperature, *J. Alloys Compd.*, 2009, **486**, p 330–334
26. J. Čížek, P. Haušild, M. Cieslar, O. Melikhova, T. Vlasák, M. Janeček, R. Král, P. Harcuba, F. Lukáč, J. Zýkad, J. Málek, J. Moon, and H.S. Kim, Strength Enhancement of High Entropy Alloy HfNbTaTiZr by Severe Plastic Deformation, *J. Alloys Compd.*, 2018, **768**, p 924–937
27. M.G. Poletti, C.M. McCaughey, G. Fiore, R. Goodall, and L. Battezzati, Refractory High Entropy Alloys: CrMoNbTiVWZr and $\text{Al}_x\text{Cr}_y\text{NbMoTiV}_z\text{Zr}_y$ ($x = 0, 0.6; y = 0.3, z = 0, 0.6$), *Int. J. Refract. Metal Hard Mater.*, 2018, **76**, p 128–133

Publisher's Note Springer Nature remains neutral with regard to jurisdictional claims in published maps and institutional affiliations.